Available online at https://link.springer.com/journal/42241
http://www.jhydrodynamics.com
Journal of Hydrodynamics, 2025, 37(1): 35-49
https://doi.org/10.1007/s42241-025-0004-7

Numerical simulations of breaking waves generated by a 3-D submerged hydrofoil

Yu-ming Shao[1], Wen-tao Wang[1, 2], Geng-lu Zhang[3], Jian-hua Wang[1*], De-cheng Wan[1]
1. *Computational Marine Hydrodynamic Lab (CMHL), School of Ocean and Civil Engineering, Shanghai Jiao Tong University, Shanghai 200240, China*
2. *China Ship Scientific Research Center, Wuxi 214082, China*
3. *Ningbo Pilot Station, Ningbo Dagang Pilotage Co., Ltd., Ningbo 315100, China*

(Received November 12, 2024, Revised November 20, 2024, Accepted November 21, 2024, Published online March 25, 2025)

Abstract: Underwater structures near the water surface can induce disturbances, leading to wave breaking, which involves complex physical mechanisms. Building on previous studies, this paper conducts a 3-D simulation of breaking waves generated by a NACA0012 hydrofoil at different angles of attack. In contrast to earlier studies, which mostly concentrated on the hydrofoil's macro-physical parameters like lift and drag, this study focuses on the dynamics of entrained bubbles after free surface breaking. The results indicate that at higher angles of attack, bubbles are swept to greater depths, and both the number and volume of the bubbles increase. By analyzing the bubble velocity data, it is found that the underwater bubble motion is primarily dominated by longitudinal movement, while transverse and vertical bubble velocities are symmetrically distributed. Additionally, vortex structures in the flow field are investigated using the third-generation vortex identification method, Liutex-Omega. It is observed that the vortex structures in the hydrofoil's wake interact with those generated by free surface breaking downstream, reducing the survival time of large bubbles and increasing the number of small bubbles. Consequently, the bubble number density power law exponent shifts from −10/3-−9/2 as bubble radius increases.

Key words: Breaking waves, submerged hydrofoil, air entrainment, bubble dynamics, free-surface flows

0. Introduction

Wave breaking is a natural phenomenon[1-2] widely observed in both the natural environment and engineering field, playing a crucial role in ocean dynamics and air-sea interactions. When the wave crest exceeds its maximum height, the wave can no longer maintain the stability of its surface, leading to the overturning and subsequent breaking of the wave. In the field of marine engineering, wave breaking impacts the performance and structural integrity of marine structures. However, due to the transient and turbulent nature of wave breaking[3-4], research into its mechanisms has remained challenging, particularly in understanding the dynamic characteristics of bubbles generated post-breaking.

Project supported by the National Natural Science Foundation of China (Grant Nos. 52131102, 52471335).
Biography: Yu-ming Shao (1998-), Male, Ph. D.,
E-mail: yuming_shao@sjtu.edu.cn
Corresponding author: Jian-hua Wang,
E-mail: jianhuawang@sjtu.edu.cn

Wave breaking research can be divided into two main kinds, depending on whether the presence of structures. In studies focusing on pure wave breaking, researchers aim to reveal patterns governing this phenomenon. Stokes[5] theoretically derived that the apex angle of a traveling wave's crest is 120°, and the critical steepness for wave breaking is 0.442, revealing the relationship between wave steepness and energy density during the breaking process. For the turbulence and bubbles generated after wave breaking, experimental methods remain the primary approach to investigating this complex phenomenon. For example, underwater acoustic instruments can measure noise signals produced by bubbles entrained in breaking waves, allowing the indirect determination of the bubbles' resonance frequency and radius. Cartmill et al.[6] used sonar technology to measure bubbles with diameters ranging from 30 μm-1 200 μm in a tank, showing that the bubble radius distribution follows a power law with an exponent of −3. However, acoustic measurements often exhibit significant errors in void fraction calculations due to challenges in defining control volumes. As a result, advanced optical

instruments such as high-definition cameras have been increasingly applied to wave-breaking studies. Deane et al.[7] investigated the size distribution of bubbles during wave breaking. They found that for bubbles larger than 1 mm, turbulent shear predominantly influences the bubbles, with the number density and radius following a −10/3 power law. For smaller bubbles, under 1 mm in size, which are mainly produced by jet and droplet impacts on the free surface, the number density and radius follow a –3/2 power law. With advances in numerical techniques and computational resources, exploring the dynamic characteristics of wave breaking through computational fluid dynamics (CFD) has become feasible. Wang et al.[8] simulated the 3-D wave breaking process using direct numerical simulation (DNS), capturing four distinct bubble entrainment mechanisms and examining the micro-scale features of splashing droplets. However, this study employed a uniform grid with 1.2×10^{10} grid points. A more efficient strategy would involve adaptive mesh refinement (AMR) technology. Mostert et al.[9] utilized AMR combined with DNS to investigate the effects of Reynolds and Bond numbers on energy dissipation, bubbles, and droplets in deep-water wave breaking.

In studies on wave breaking induced by structures, the most common condition involves structures penetrating the free surface. Liu et al.[10] experimentally investigated the bow wave-breaking phenomenon of a KCS ship model under different scale ratios and trim angles. However, their analysis was limited to macroscopic quantities such as drag and wave height, without addressing smaller-scale structures like jets and cavities generated by wave breaking. Hu et al.[11-12] numerically simulated wave breaking caused by a plate penetrating the free surface. Their study not only examined macroscopic quantities such as wave height, crest position, and wave profile distribution, but also quantitatively analyzed small-scale structures including thin liquid films, jets, droplet splashes, and the distribution of entrained bubbles during the breaking process. Li et al.[13] conducted simulations on the hydraulic jump phenomenon caused by a hydrofoil penetrating the free surface. Using the coupled level set and volume of fluid (CLSVOF) interface capturing method, combined with a mass-momentum consistent advancing strategy[14], they enhanced the stability of high-density ratio two-phase flows, successfully providing a quantitative description of the highly turbulent two-phase mixing region in the hydraulic jump area. Hendrickson et al.[15-16] studied the flow structures and large-scale air entrainment in the wake of a transom-stern ship. They found that the region with the strongest air entrainment coincided with the wave-breaking region. Additionally, they developed a model to predict turbulence in incompressible highly variable-density regions by utilizing the mean density gradient and buoyancy. Zhang et al.[17] further reviewed the numerical approach in simulating the bubble flows around ship and offshore structures.

For fully submerged structures, wave breaking can occur when the structure is sufficiently close to the water surface. For instance, in the case of a cylinder[18-20], Guo et al.[21] investigated free surface breaking induced by a rotating cylinder in a 2-D condition. They discussed various flow structures, including the dynamic behavior of the cylinder, force coefficients, rotational structures, and air entrainment under different Froude numbers and rotation ratios. Regarding submerged hydrofoils, previous studies[22-24] have primarily focused on the forces acting on the hydrofoil and whether wave breaking occurs, without examining phenomena such as bubble entrainment. Murai et al.[25] conducted experimental measurements in a towing tank to investigate bubble drag reduction on a model ship, focusing on bubble formation after free surface breaking induced by the hydrofoil. They discovered that the anti-stall characteristics and the cancellation of vertical pressure gradients in the hydrofoil are dependent on the Froude number, leading to three distinct bubble generation mechanisms. This further demonstrated the advantages of bubble generation devices on hydrofoils for high-speed vessels. Shao et al.[26] performed simulations of free surface breaking induced by a hydrofoil at different submergence speeds in a 2-D setting. They studied the energy dissipation caused by wave breaking and extracted the spatiotemporal distribution of bubbles, identifying three distinct entrainment mechanisms and the characteristics of bubble. However, they also noted that the 3-D motion of bubbles made 2-D simulations insufficient for a comprehensive analysis of bubble behavior following wave breaking.

This paper builds upon previous research[26] to investigate free surface breaking and bubble dynamics induced by a hydrofoil in the 3-D condition. Our primary focus is on the changes in the flow field, rather than macroscopic quantities such as the forces acting on the hydrofoil.

1. Numerical method

1.1 *Governing equations*

This study is based on the open-source multi-phase flow solver Basilisk, which has been validated through simulations of physical phenomena such as jets and pure wave breaking[26]. The governing equations can be written as follows:

$$\rho\left[\frac{\partial \boldsymbol{U}}{\partial t}+(\boldsymbol{U}\cdot\nabla)\boldsymbol{U}\right]=-\nabla p+\nabla\cdot(2\mu\boldsymbol{D})+\rho\boldsymbol{g}+\boldsymbol{F}_{\sigma} \quad (1)$$

$$\nabla \cdot \boldsymbol{U} = 0 \tag{2}$$

where $\boldsymbol{U}$ is the velocity field, ρ is the density, p is the pressure, μ is the fluid dynamic viscosity, D_{ij} is the deformation tensor, $\boldsymbol{g}$ is the gravitational acceleration and $\boldsymbol{F}_\sigma$ accounts for surface tension effects. The approximate projection method is employed for discretization. The convective terms are discretized using the second-order upwind Bell-Collela-Glaz scheme, while the diffusive terms are handled with the second-order Crank-Nicholson scheme.

1.2 *Free surface capturing*

To better capture the free surface, the VOF-PLIC coupled level set method, known as CLSVOF is employed in this study. This approach offers advantages such as mass conservation and accurate representation of interface geometry.

$$\partial_t f + \nabla \cdot (f\boldsymbol{U}) = 0 \tag{3}$$

$$\partial_t \phi + \nabla \cdot (\phi \boldsymbol{U}) = 0 \tag{4}$$

where f is the volume fraction field in the VOF method, ϕ is the distance function field in the level set method.

Surface tension is crucial for bubble breakage and coalescence. Surface tension is modeled using an improved balanced-force continuum surface force (CSF) model, and local curvature is calculated using the height function (HF) method[27].

$$\boldsymbol{F}_\sigma = \sigma\kappa(f)\delta_s \boldsymbol{n} \tag{5}$$

where σ is the surface tension coefficient, κ isthe curvature of the free surface, δ_s is the Dirac function of the interface and $\boldsymbol{n}$ is the surface normal.

To account for the pressure jump condition near the free surface, the ghost fluid method (GFM) is employed to address the spurious velocity issue in high-density ratio two-phase flows. Capturing bubble dynamics requires a large number of fine grids, making the use of adaptive mesh refinement (AMR) essential. The AMR technique refines and coarsens the mesh by using a wavelet algorithm to assess the error in physical quantities. In this study, the maxi-mum tolerance is set to $u_{\text{err}} = v_{\text{err}} = w_{\text{err}} = 0.1$ for the velocity field and $f_{\text{err}} = 1\times10^{-18}$ for the volume fraction field. Further details can be found in the paper[28].

1.3 *Liutex vortex identification method*

Liutex is a third-generation vortex identification method[29-30] developed in recent years. Compared with first-generation method (vorticity), Liutex can accurately identify vortex structures and provide correct vortex cores and boundaries. Unlike second-generation methods (Q, Δ, λ_2, λ_{ci}), it can also offer information on the local rotation axis and resolve issues related to threshold selection.

Table 1 Liutex calculation steps in the Basilisk Flow Solver

	Calculation procedure
1	Initialize the global vector $\boldsymbol{R}$, scalar Ω_R
2	**for** each cell in mesh **do**
3	Calculate the velocity gradient tensor $\boldsymbol{J}$
4	Calculate the eigenvalues and eigenvectors
5	**if** a real root and a pair of conjugate virtual roots **then**
6	Calculate rotation matrix Q
7	Calculate velocity gradient tensor $\boldsymbol{J}' = Q\boldsymbol{J}Q^{\mathrm{T}}$
8	Calculate α, β
9	Compute Liutex $\boldsymbol{R}$, Ω_R
10	**end if**
11	**end for**

The steps for solving Liutex vortex structures in the Basilisk flow solver are presented in Table 1, with particular emphasis on the normalized Liutex-Omega method:

$$\Omega_R = \frac{\beta^2}{\beta^2 + \alpha^2 + \lambda_{cr}^2 + 0.5\lambda_r^2 + \varepsilon} \tag{6}$$

$$\alpha = 0.5\sqrt{(J'_{11} - J'_{22})^2 + (J'_{21} + J'_{12})^2} \tag{7}$$

$$\beta = 0.5(J'_{21} - J'_{12}) \tag{8}$$

where λ_{cr}, λ_r are the real part of the conjugate complex eigenvalues and the real eigenvalues of the velocity gradient tensor, the term $\varepsilon = b_0 \max(\beta^2 - \alpha^2, 0)$ is used to avoid the division by zero problem and $b_0 = 10^{-6}$ is a small constant. The recommended value of 0.52 is used for Ω_R in this paper.

2. Computational set-up

2.1 *Physical model*

The schematic diagram of the computational domain is shown in Fig. 1. The hydrofoil used in this study is the NACA0012, with a chord length of $c = 1\,\text{m}$ and submergence depth h. The computa-

tional domain is a rectangular region with dimensions $8c \times 8c \times 0.25c$. The inlet is located at $x = -2c$ and is set as a velocity inlet boundary. The outlet is positioned at $x = 6c$, defined as a pressure outlet boundary. The top and bottom, located 4c above the hydrofoil, are set with a no-slip boundary condition, while the front and back boundaries are treated as symmetric. For more details, please refer to the previous study[26].

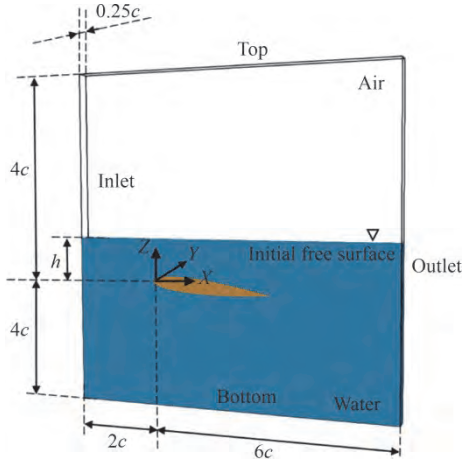

Fig. 1 The computational domain

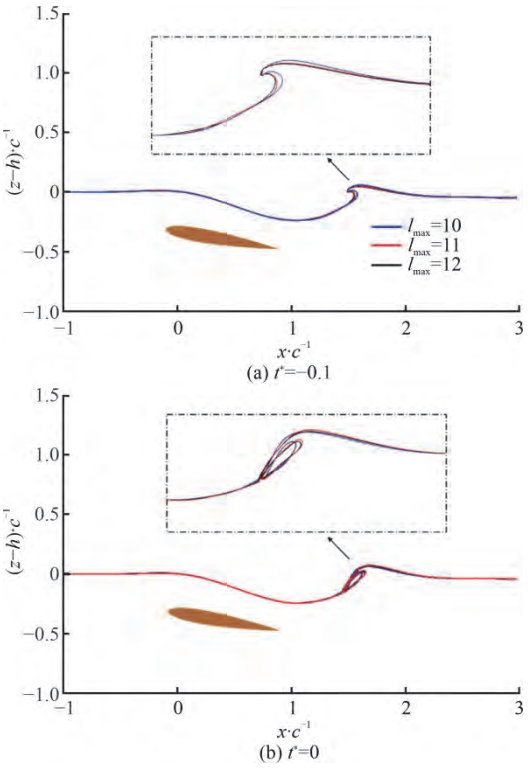

Fig. 2 Instantaneous free surface in case 2

In this research, four different cases with varying submergence depths and angles of attack are designed, as shown in Table 2. The density ratio between air and water is $\rho_a / \rho_w = 1/998$, and the dynamic viscosity ratio is $\mu_a / \mu_w = 1.784 \times 10^{-5} / 1.138 \times 10^{-3}$. The gravitational acceleration is $g = 9.81\ \mathrm{m/s^2}$, and the surface tension coefficient is $\sigma = 0.072$ N/m. The inflow velocity is set to $U_0 = 1.789\ \mathrm{m/s}$, corresponding to a Reynolds number $Re = \rho_w U_0 c / \mu_w = 1.569 \times 10^6$. For better comparison across cases, the dimensionless time is used, $t^* = (t - t_0) U_0 / c$, where t is the computation time, t_0 is the time of the first cavity entrainment.

Table 2 Simulation conditions

Condition	h/c	Angle of attack/°
Case 1	0.3	5
Case 2	0.3	10
Case 3	0.3	15
Case 4	1.3	10

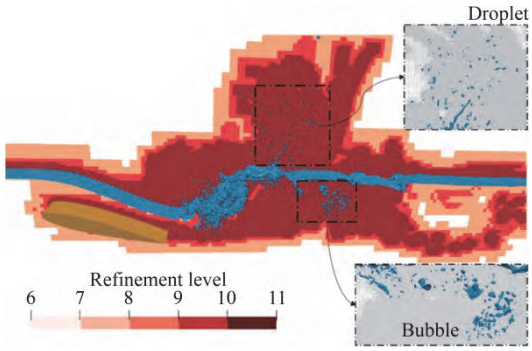

Fig. 3 Schematic diagram of grid adaptive refine- ment strategy

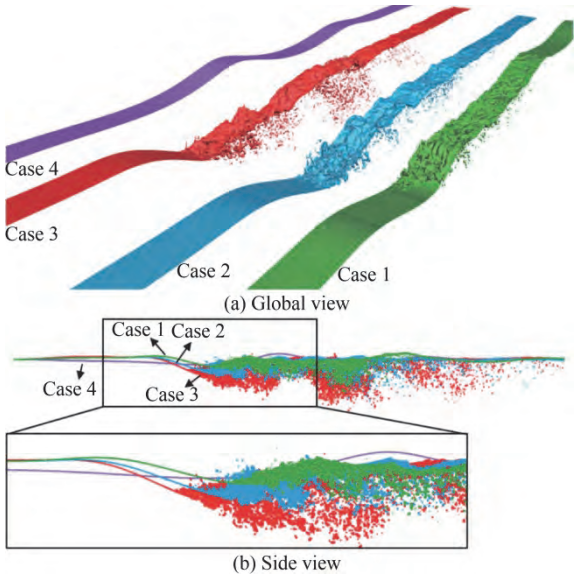

Fig. 4 Comparison of wave profiles at $t^* = 8$

2.2 *Grid sensitivity analysis*

Due to the use of adaptive mesh refinement, it is

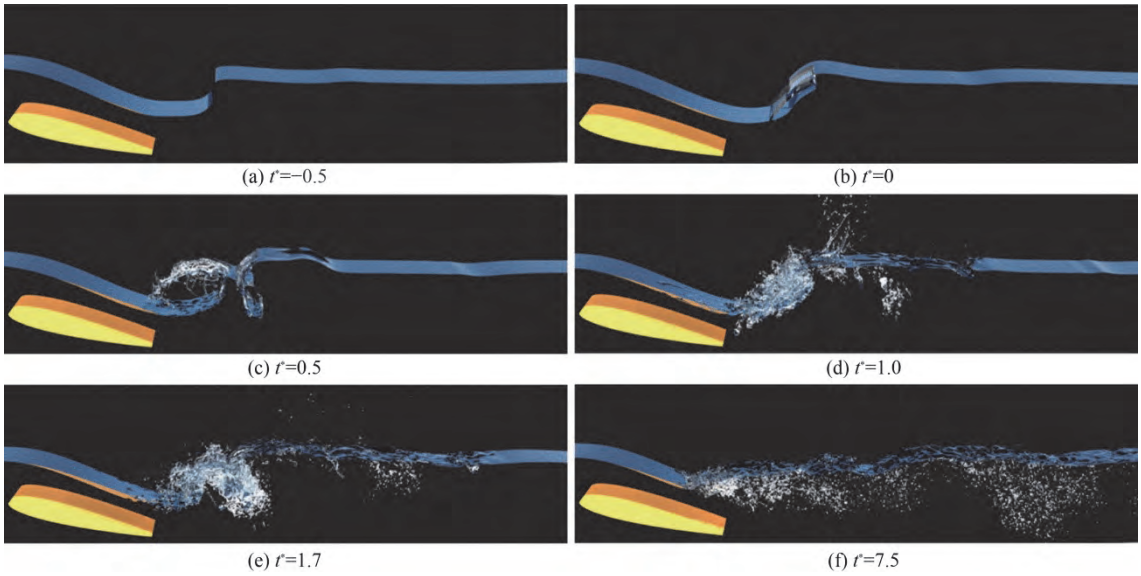

Fig. 5 Wave breaking development process in case 3

necessary to define mesh refinement levels. In this study, the minimum refinement level is set to 6. Three maximum refinement levels, $l_{\max}$ = 10, 11, 12, corresponding to minimum grid sizes of $\Delta_{\min} = c/128$, $c/256$, $c/512$, are implemented for the mesh sensitivity analysis. Figure 2 shows the moment of air cavity formation caused by the first wave breaking in case 2. From the figures, it can be observed that the free surface shapes captured at the three maximum refinement levels are largely similar, with the main differences occurring at the wave front just before breaking and at the front and rear ends of the entrained air cavity. Comparing the results, the refinement levels $l_{\max} = 11, 12$ show closer agreement, while the coarser grid at $l_{\max} = 10$ exhibits slight discrepancies.

To balance the number of grid cells and the computational resource requirements, the refinement level $l_{\max} = 11$ is selected for this study. Figure 3 illustrates the distribution range of grid adaptive refinement levels. From the figure, it can be seen that the region with significant free surface variation is refined to the maximum level. Additionally, areas around the hydrofoil and in the wake, where there are large velocity gradients, are also refined to the highest level. The current mesh resolution is capable of capturing the droplet splashing and the bubble sweep-down during the wave breaking process.

3. Results and discussions

3.1 *Wave breaking process*

From the global view in Fig. 4(a), wave breaking occurs in case 1-3, where significant deformation in the leading wave region and entrained bubbles below the free surface can be clearly observed. In case 4, due to the larger distance between the hydrofoil and the free surface, the surface exhibits a regular undulating pattern without any breaking. In the side view presented in Fig. 4(b), for case 1-3, it is evident that as the angle of attack increases, the leading wave region depresses further, with more entrained bubbles and a greater maximum depth of bubble penetration. Comparing cases 2, 4, both with a 10° angle of attack, it can be seen that the first wave crest in case 4 is positioned further downstream and has a higher peak. The leading wave in case 4 does not exhibit significant depression, whereas in case 1-3, the wave profile in the leading wave region initially rises sharply before forming a deeply depressed breaking zone.

Figure 5 illustrates the evolution of the free surface for case 3, which has the most intense wave breaking with a 15° angle of attack. At $t^* = -0.5$, due to the influence of the hydrofoil, the depression forms above the hydrofoil on the free surface, generating a velocity difference. This causes water to accumulate at the first wave crest, continuously increasing in wave height. At $t^* = 0$, the steepness of the leading wave exceeds the threshold, causing the wave crest to overturn in the upstream direction. After closing with the free surface, the first large air cavity is entrained. At $t^* = 0.5$, the leading wave region retains significant kinetic energy, forming a water tongue that continues to roll forward. At $t^* = 1.0$, the water tongue impacts the free surface, generating a highly mixed air-water region and producing splashing droplets above the

surface. The underwater air cavity breaks into larger bubbles, with some escaping the free surface while others move downstream. At $t^* = 1.7$, the leading wave continues to break, forming a larger entrained air cavity, while the first air cavity has already broken into smaller bubble clusters. At $t^* = 7.5$, the free surface has stabilized into a continuous breaking pattern, with the leading wave repeatedly breaking and entraining air, and numerous small bubbles distributed underwater. The entire breaking process resembles a hydraulic jump phenomenon[13], driven by velocity differences that create shear-induced breaking in the opposite direction of the flow.

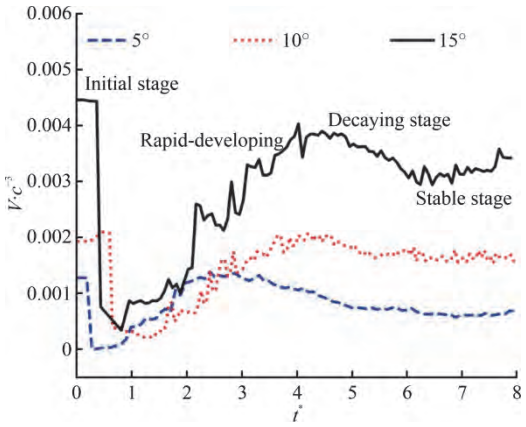

Fig. 6 The curve of the air volume over time

3.2 *Evolution of entrapped bubble clouds*

The curves of air volume for the three wave-breaking conditions, case 1-3, are shown in Fig. 6. It can be observed that the entrained bubble volume for all three cases initially decreases sharply, then increases to a peak, followed by a slight decline and stabilization. Taking the 15° angle of attack as an example, for $t^* \leq 1$, during the initial stage, the free surface undergoes its first overturn, entraining a large air cavity. This cavity quickly breaks apart and escapes the surface, causing the bubble volume to drop sharply from a high value to the lowest point. For $1 < t^* \leq 4$, the bubble volume enters the rapid-developing stage. During this period, the free surface continuously breaks, entraining large amounts of air into the water. Although large bubbles escape, causing slight fluctuations in the curve, the overall trend shows an increase. For $4 < t^* \leq 6$, larger bubbles in the flow field either break into smaller ones or escape to the surface, causing a slight decrease in bubble volume. After $t^* > 6$, the bubble volume enters the stable stage, maintaining a relatively constant value. Compared with the three cases, it is evident that the larger the hydrofoil angle of attack, the larger the initial entrained air cavity volume. Additionally, the rapid development stage lasts longer, with a higher peak, and the total bubble volume remaining in the water during the stable stage is greater.

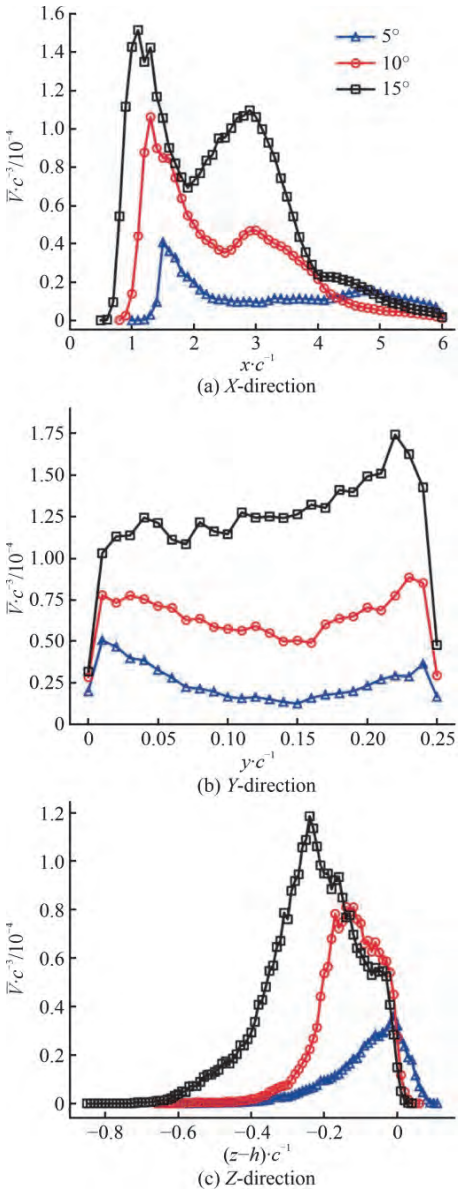

Fig. 7 Spatial distribution of time-averaged air volume

Figure 7 shows the spatial distribution of the time-averaged bubble volume between $6 < t^* \leq 8$. Overall, a larger hydrofoil angle of attack induces greater air entrainment. From Fig. 7(a), it can be observed that there are two peak regions along the X-direction. The first peak region, located between $1 < x/c < 2$, corresponds to the leading wave region, where the free surface breaks most intensely, leading to the greatest air entrainment. The second peak occurs around $x/c = 3$, where some of the bubbles originate from the upstream region, while another portion results from the free surface in this area breaking due to the

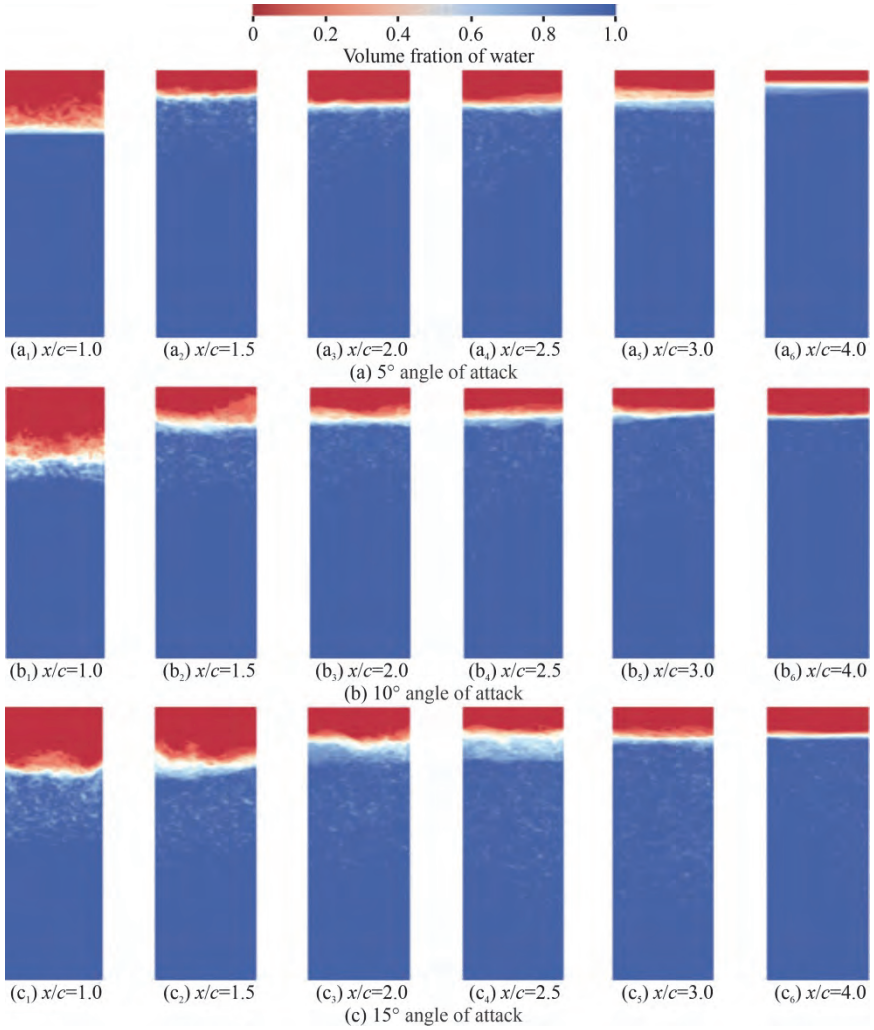

Fig. 8 Time-averaged void fraction contours in the Y - Z plane

influence of the leading wave, thus entraining more air. In Fig. 7(b), the bubble distribution in the Y - direction shows a concave shape, with lower volumes in the middle and higher volumes on both sides. This is attributed to the symmetric boundary conditions imposed on both Y - boundaries, restricting the horizontal flow of bubbles. In Fig. 7(c), it can be observed that with increasing depth, the bubble volume initially increases and then decreases. Additionally, the greater the hydrofoil angle of attack, the deeper the bubble penetration into the water.

Figure 8 shows the time-averaged volume fraction field in the Y - Z plane. It can be observed that wave breaking is significantly influenced by the front and back boundary conditions, displaying a concave shape, similar to the pattern in Fig. 7(b). At $x/c = 2.5$, the free surface breaking is relatively weak for the 5°, 10° angle of attack cases, whereas for the 15° case, a larger breaking region persists. This further illustrates that a larger angle of attack leads to a greater scale and extent of free surface breaking. In addition, it is evident that as the angle of attack increases, more bubbles are entrained, and the depth of bubble penetration deepens.

The temporal evolution of the bubble cloud center is further extracted, as shown in Fig. 9. Figure 9(a) depicts the distribution of the bubble cloud centroid in the X - direction. For the 5° case, the centroid increases to a peak and then decreases, which is due to the smaller number and volume of bubbles that dissipate around $x/c = 3.5$ after drifting away from the hydrofoil. For the 10°, 15° cases, two peaks are observed. The first peak is primarily due to the large air cavity formed during the initial breaking process. This air cavity escapes from the free surface near $x/c = 2$ as it flows downstream. Subsequently, as these two cases exhibit a larger number of bubbles persisting in the water, the bubble cloud centroid continues to move downstream. In Fig. 9(b), the bubble cloud centroid in the Y - direction shows minimal movement, with the centroid remaining

mostly symmetric around $y/c=0.125$, indicating that bubble movement in the Y-direction is not significant. Figure 9(c) illustrates the centroid distribution in the Z-direction, where each curve reaches a peak before decreasing and eventually stabilizing. This peak is caused by the temporary presence of the large air cavity near the free surface. As the flow evolves, the bubbles stabilize in the underwater region. It is also evident here that a larger hydrofoil angle of attack results in deeper bubble penetration.

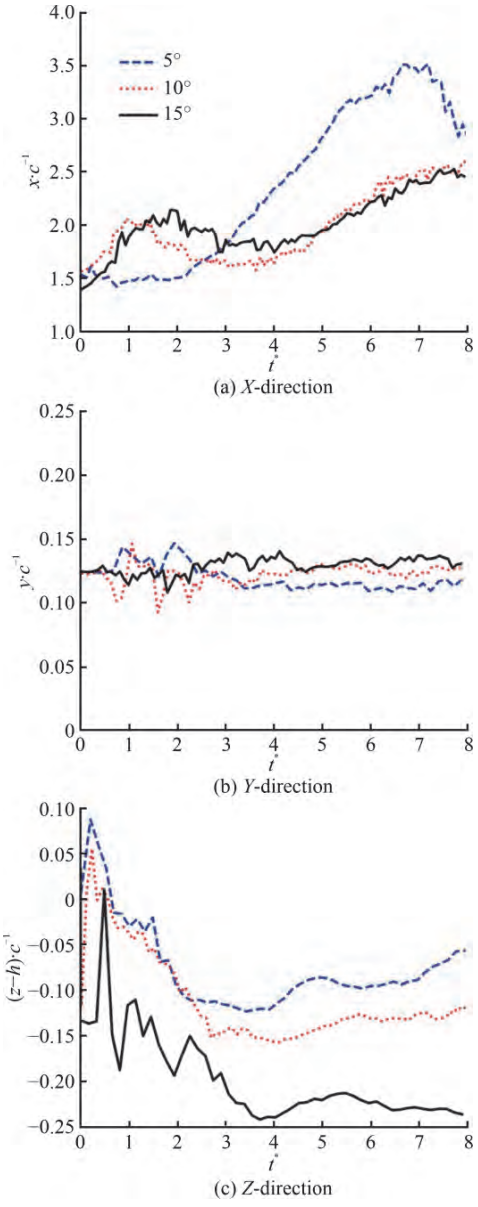

Fig. 9 Time histories of the distribution of bubble cloud center

3.3 *Distribution of bubble size*

Figure 10 shows the variation of the bubble number over time. For $t^*\le 6$, the bubble number continuously increases. For the 5° angle of attack case, during the stable stage $t^*>6$, there is a slight decrease in the bubble number. In contrast, for the 10°, 15° cases, the bubble number in the region shows a slower growth trend. Comparing the three curves, it is clear that the larger the hydrofoil's angle of attack, the greater the number of entrained bubbles.

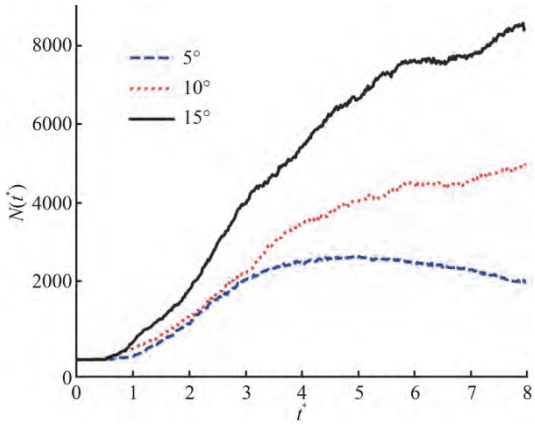

Fig. 10 The curve of the bubble number over time

Figure 11 shows the bubble size distribution for the 15° angle of attack case, where $N(r_{\text{eff}},t^*)$ represents the number of bubbles, corresponding to the equivalent radius $r_{\text{eff}}=(3V/4\pi)^{1/3}$ in the entire computational domain. For $t^*\le 1$, there are only a few large air cavities in the flow field. For $1<t^*\le 4$, both small and large bubbles increase rapidly, with a relatively uniform size distribution. During the dissipation stage $4<t^*\le 6$, many large bubbles break into smaller ones, and bubbles with $r_{\text{eff}}/c\le 5$ show a clear increasing trend. For $t^*>6$, the flow field stabilizes, the total bubble number peaks, and the size distribution shows that the smaller the bubble, the higher its number.

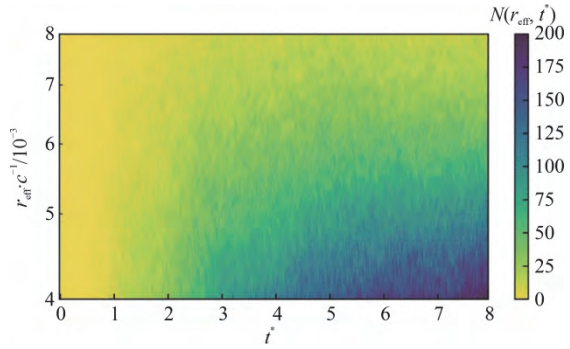

Fig. 11 Contours of bubble size distribution

During the air entrainment process, bubbles of various sizes generated by wave breaking aggregate, forming a macroscopically visible bubble cloud. Figure

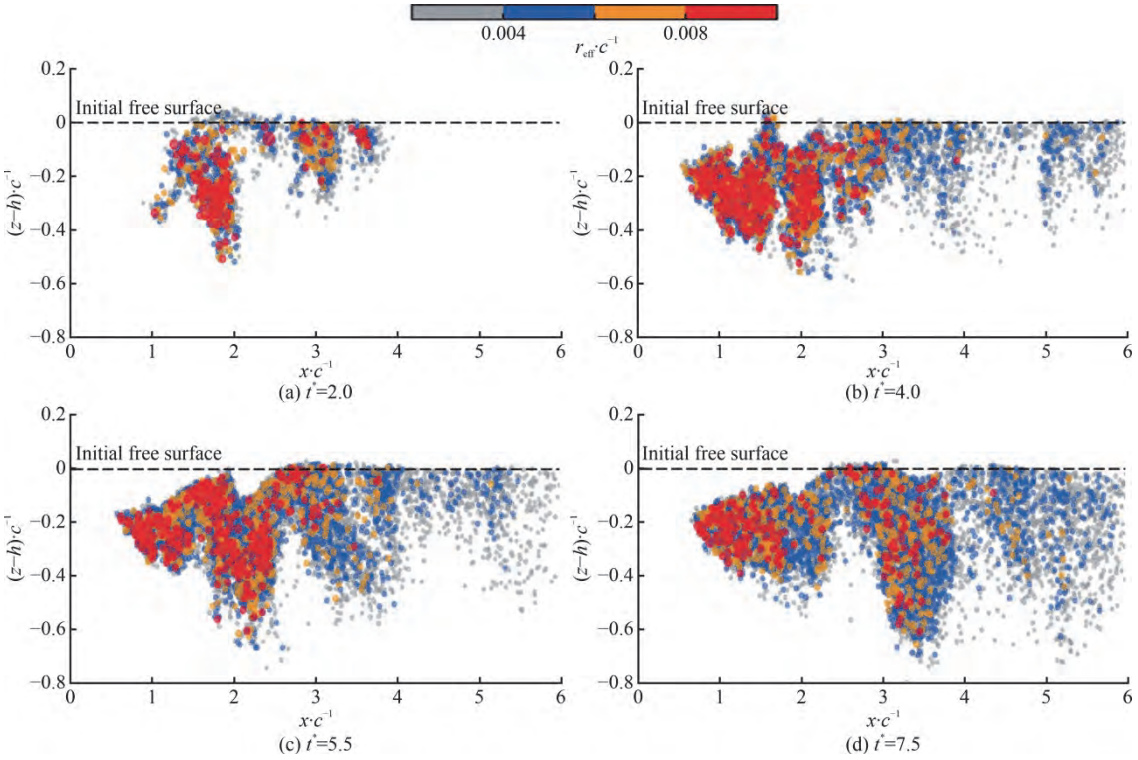

Fig. 12 Time evolution of the spatial distribution of bubbles underwater in X - Z plane

12 illustrates the time evolution of bubble distribution in the X - Z plane under the condition of a 15° angle of attack. In Fig. 12(a), representing the end of the initial bubble volume stage, the total bubble volume is at its lowest. A few large bubbles still dominate, with the first entrained air cavity at $x/c=3$, which has already broken up into numerous smaller bubbles. At $t^*=4$, which marks the end of the rapid development stage, the total bubble volume reaches its peak. As seen in Fig. 12(b), a significant number of large bubbles remain present in the leading wave region. At $t^*=5.5$, during the dissipation stage, Fig. 12(c) reveals the formation of a distinct bubble cloud near $x/c=2$, which contains many large bubbles. At $t^*=7.5$, during the stable stage, Fig. 12(d) shows that the bubble cloud observed in Fig. 12(c) has shifted to approximately $x/c=3.5$. At this point, the larger bubbles within the cloud have fragmented, and smaller bubbles now predominate. Throughout all stages of development, the leading wave breaking region in $1<x/c<2$ serves as the primary source of entrained air in the flow field, with most large bubbles being generated.

Figure 13(a) presents the instantaneous results of the bubble number density spectrum for the 15° angle of attack case. The figure indicates that as the flow field evolves, the number of small bubbles gradually increases while the number of large bubbles

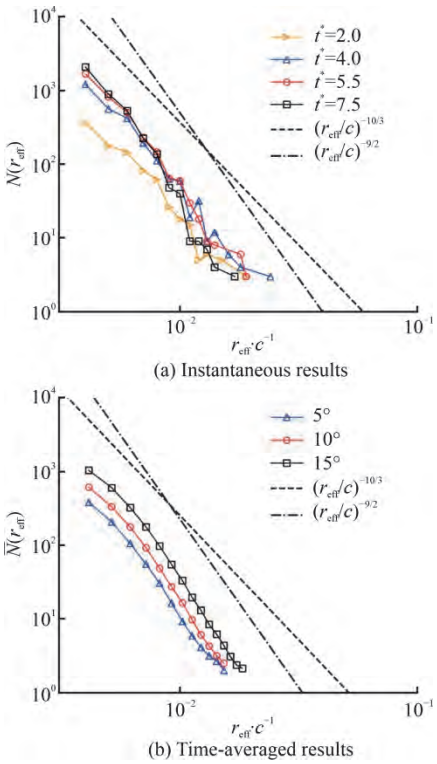

Fig. 13 Bubble number density spectrum

decreases, leading to an increase in the slope of the curve. The power-law exponent changes from –10/3-

–9/2[11, 31]. This shift is primarily due to the disturbance caused by the hydrofoil, which shortens the lifespan of large bubbles in the flow[13]. Figure 13(b) shows the time-averaged results for all three cases during the period of $6 \le t^* \le 8$. It can be observed that the trend in the bubble density spectrum is highly consistent across the three cases, with the power-law exponent consistently transitioning from –10/3-–9/2. This suggests that the bubble size distribution undergoes a regular change due to the influence of the hydrofoil on the air entrainment caused by free surface breaking.

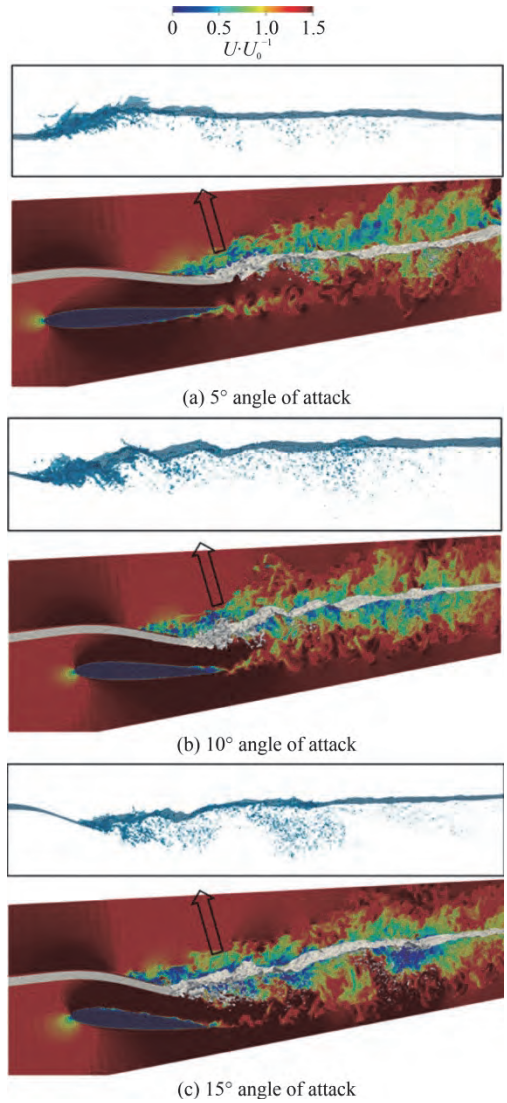

Fig. 14 Instantaneous velocity field at $t^* = 8$

3.4 *Distribution of bubble velocity*

Figure 14 illustrates the velocity field at $t^* = 8$. It reveals that the wake velocity fields behind the hydrofoil vary depending on the angle of attack. At a 5°, vortex-like oscillations in the wake can still be observed. However, at 10°, 15°, no distinct wake shedding is visible, and the hydrofoil wake rapidly mixes with the velocity field near the free surface downstream. By comparing with the free surface images, it is evident that both the underwater velocity field and the wake region of the hydrofoil contain numerous bubble clusters. This indicates that the bubbles' velocities are influenced not only by the shear-induced breakup at the free surface but also by the hydrofoil's wake.

Figure 15 depicts the bubble motion during the stable stage. The bubble cloud can be divided into three regions: I, II, III. Region I corresponds to the area where wave breaking is most intense, and it contains the largest bubbles. In this region, bubbles exhibit low velocities and shallow downward penetration. Initially, the bubbles are entrained into the water with a downward trajectory, but due to the buoyancy of the larger bubbles, they quickly shift upward. Region II contains the highest concentration of bubbles, showing significant bubble clustering. Most large bubbles in this region have already fragmented, and the velocity patterns show a downward-to-upward trend, influenced by both the free surface breaking and the hydrofoil's vortex wake. Region III has the fewest bubbles, with a relatively stable free surface. As this region is far from the hydrofoil, the flow field has stabilized. Large bubbles have either fully fragmented or escaped, leaving small bubbles, which dominate and move slowly downstream.

The variation of bubble velocities over time is illustrated in Fig. 16. In Fig. 16(a), it is shown that for $t^* \le 1$, the number of bubbles is relatively small, and the distribution of bubbles across different velocities is fairly uniform. For $1 < t^* \le 4$, most bubble velocities fall within the range of $0.25 \le U / U_0 \le 1$, with higher-velocity bubbles slightly decreasing. In the interval of $4 < t^* \le 6$, the bubbles with similar velocities become more concentrated, and low-velocity bubbles slightly increase, with the distribution narrowing to $0.13 \le U / U_0 \le 0.9$. After $t^* > 6$, the bubble velocity distribution remains similar to the previous stage, with a significant number of bubbles concentrated around $U / U_0 = 0.6$.

Figure 16(b) shows the distribution of bubble velocities in the X-direction. The pattern closely resembles that of Fig. 16(a), and the velocity magnitude in the X-direction is clearly greater than that in the Y-, Z-directions. This indicates that bubble velocity in the X-direction dominates throughout the flow evolution. During $t^* \le 4$, as the free surface breaking is still developing and the wave-breaking process opposes the incoming flow, the bubbles entrained have relatively large negative velocities in the X-direction. For $4 < t^* \le 6$, the negative velocity magnitude in the X-direction decre-

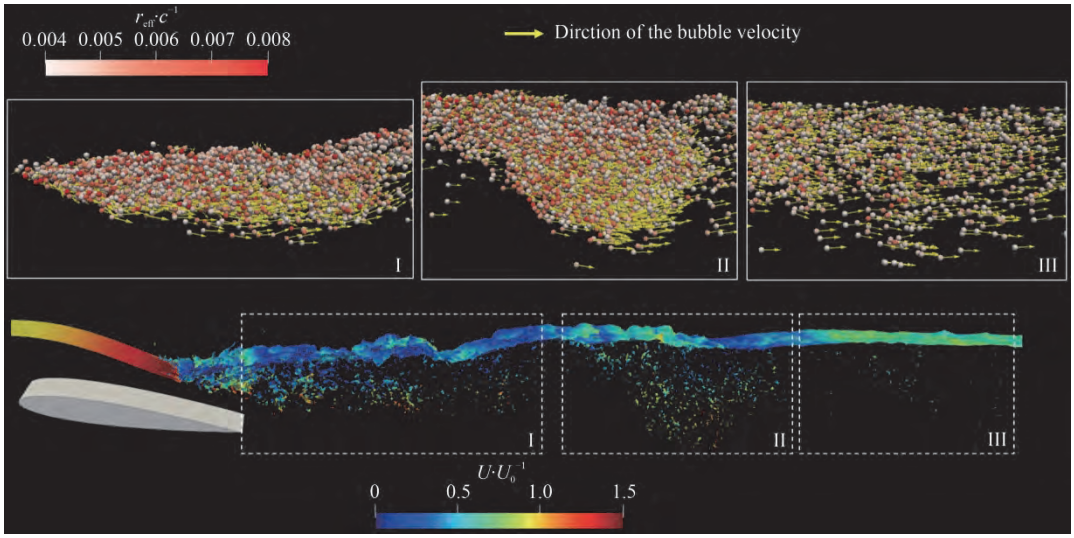

Fig. 15 The diagram of bubble motion

ases, and most bubbles are concentrated within the range of $0 \le u/U_0 \le 1$. After $t^* > 6$, as the flow field stabilizes, the bubble velocity in the X-direction converges around $u/U_0 = 0.6$, consistent with the total velocity trend.

For bubble motion in the Y-direction, Fig. 16(c) shows that the velocity distribution is almost symmetric around zero, indicating that the three-dimensional effects on bubble velocity are not significant. This conclusion aligns with the observation in Fig. 9(b). Figure 16(d) presents the velocity distribution in the Z-direction. In the initial stage, bubbles exhibit a downward motion tendency, but the overall distribution is symmetric about 0. This symmetry suggests that the numbers of bubbles moving downward and upward are nearly equal, reflecting the alternating downward and upward motion of bubble clouds, as also shown in Fig. 15.

To quantitatively analyze the bubble velocity distribution, the bubble number-velocity curves are presented in Fig. 17. From Fig. 17(a), it can be observed that as the flow field evolves, the overall bubble velocity exhibits an increasingly prominent inverted U-shaped distribution. The peak is mainly located between $0.25 \le U/U_0 \le 1$, consistent with the trend in Fig. 16(a). Fig. 17(b) shows the velocity distribution of bubbles in the X-direction, which also follows an inverted U-shape, with the maximum peak around $u/U_0 = 0.6$. Additionally, as the velocity increases, the curves at different times converge, indicating that bubbles with higher velocities are consistently generated during different stages of the wave-breaking process. Figure 17(c) demonstrates an inverted V-shaped velocity distribution, with the peak occurring at zero velocity. Finally, Fig. 17(d) shows that after the flow field stabilizes, the bubble velocity distribution in the Z-direction forms a symmetric inverted V-shape around zero. However, during the initial stages of flow development, the bubble velocity is biased towards upward motion.

3.5 *Typical vortex structures*

When the submergence depth is large, the free surface remains unbroken, and the vortex structures in the wake of the hydrofoil do not interact with the free surface, as shown in Fig. 18. In this case, the hydrofoil wake exhibits regular vortex shedding, with high-intensity vortex structures at the hydrofoil's top and the initial shedding region at the trailing edge. By extracting the vortex structures near the hydrofoil's top, the transition of the incoming flow from laminar to turbulent can be clearly observed, including the formation of vortex tubes in the laminar region and hairpin vortices in the turbulent region.

When the submergence depth is small, the interaction between the wake vortices and the vortex structures generated by the breaking of the free surface introduces a highly complex physical process. Figure 19 illustrates the time evolution of vortex structures for case 2. At $t^* = 0$, as the free surface first breaks and entrains air, the regular vortex shedding behind the hydrofoil begins. Fine vortex shedding can also be observed at the crest of the leading wave. At $t^* = 0.1$, multiple instances of free surface breaking occur, producing numerous splashing droplets, which also contain complex vortex structures. Strong vortex structures are present both above and below the free surface in the breaking region, and it can be seen that the trailing vortices from the hydrofoil rise towards the

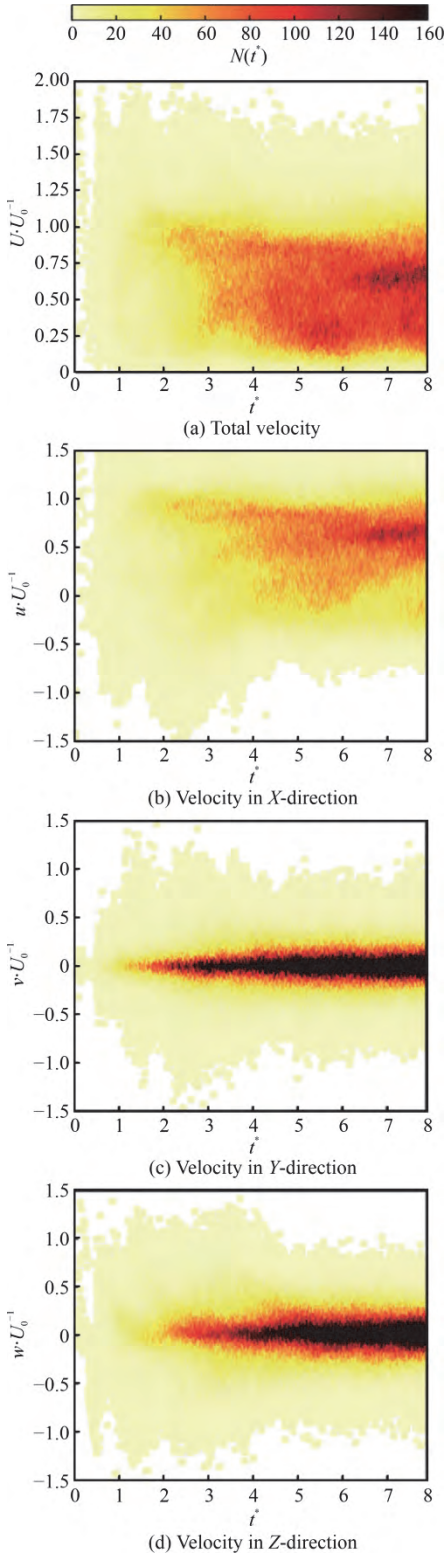

Fig. 16 Contours of bubble velocity

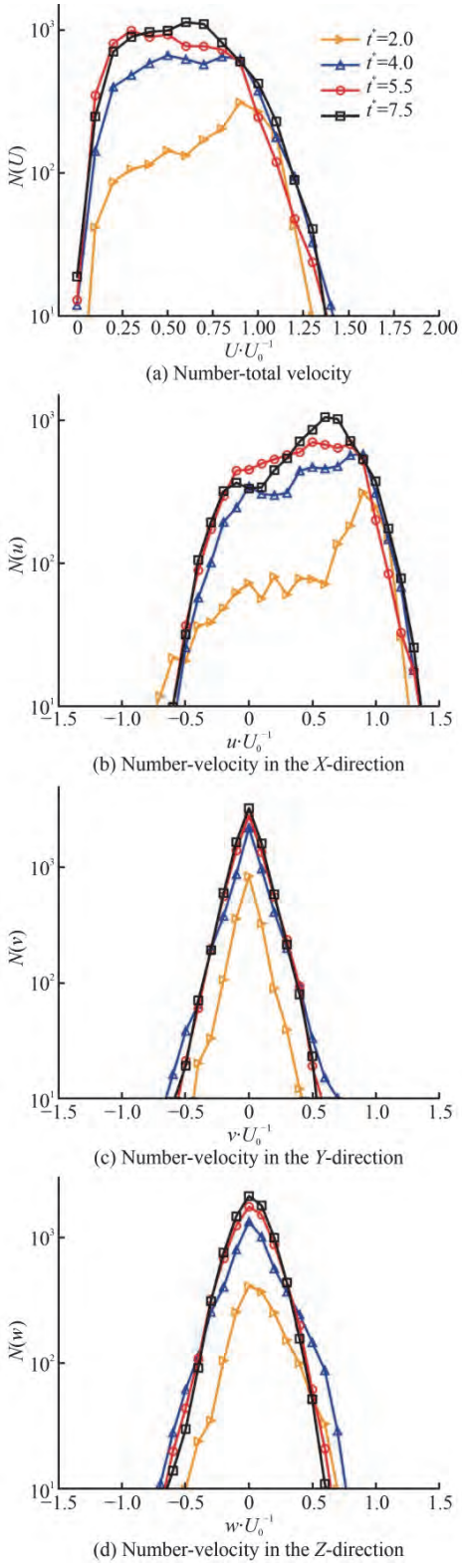

Fig. 17 The joint bubble number-velocity distribution

free surface. At $t^* = 1$, more pronounced droplet splashing vortex structures can be observed above the free surface. While underwater, the front portion of the hydrofoil wake continues to exhibit clear vortex shedding, but the rear wake has already begun to interact with the free surface. At $t^* = 7.5$, a highly complex vortex structure has formed above the water

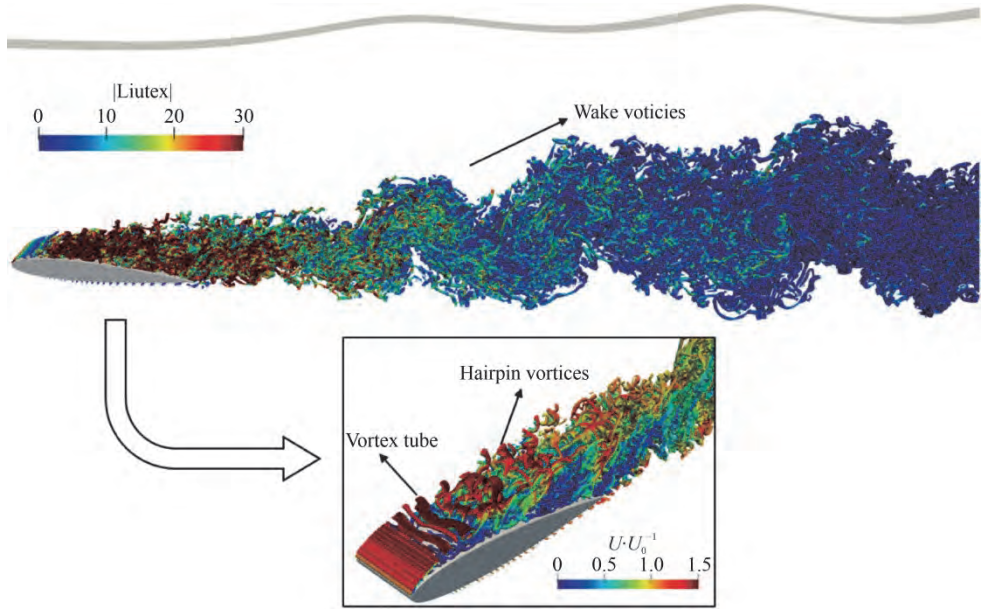

Fig. 18 Typical vortex structure in case4

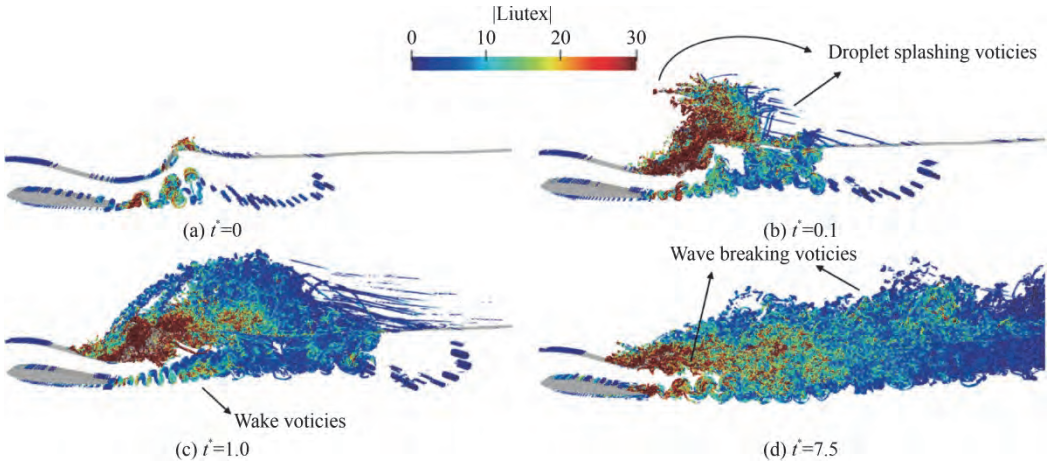

Fig. 19 Evolution of vortex structure in case 2

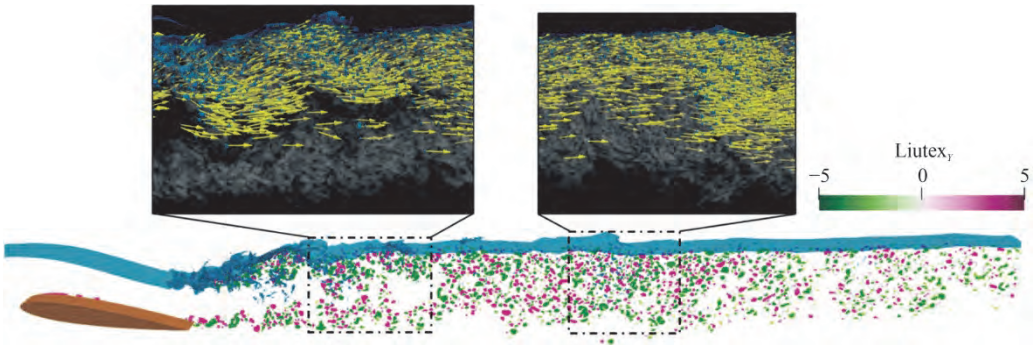

Fig. 20 The effect of vortex structure on the movement of bubbles

surface. While underwater, the hydrofoil wake is mixed with the vortices from the wave breaking, creating a chaotic and disordered vortex field. Compared with the case with large submergence, at smaller submergence depths, fewer vortex structures form at the top of the hydrofoil, and no hairpin vortices

or other turbulent transition phenomena are observed. This indicates that a significant amount of energy is dissipated through the breaking of the free surface, which suppresses the development of turbulence on the hydrofoil's surface.

Figure 20 shows the instantaneous flow field for case 2 at $t^* = 7.5$. It can be seen the initial vortex shedding from the hydrofoil wake consists of alternating positive and negative vortices. As the wake develops downstream, the vortices rise and mix with the wave-breaking vortices, eventually dissipating through the free surface. In conjunction with Fig. 15, it can be observed that in these mixed vortex regions, bubbles are entrained downstream. Large bubbles are more rapidly broken and escape, reducing their residence time, while smaller bubbles are swept to greater depths. This also explains the changes in the power-law exponent of the bubble number density spectrum, as shown in Fig. 13.

4. Conclusions

This paper presents a 3-D numerical simulation study of free surface breaking induced by a shallowly submerged hydrofoil. The primary focus is on investigating the free surface breaking at different angles of attack and analyzing the dynamics of the entrained bubbles. Key aspects explored in this study include the free surface breaking process under varying conditions, the evolution of underwater bubble clouds, bubble size distribution, bubble velocity distribution, and typical vortex structures within the flow field. The main conclusions are summarized as follows:

(1) At the same submergence depth, a larger angle of attack leads to more intense free surface breaking and a greater number of entrained bubbles.

(2) Bubbles tend to cluster underwater, forming bubble clouds. The larger the angle of attack, the larger the volume of the bubble cloud and the deeper its centroid.

(3) The majority of bubbles underwater have a size of $r_{\text{eff}} / c \le 5$. As the radius increases, the bubble number density power law exponent changes from −10/3-−9/2.

(4) The underwater bubble velocity is primarily dominated by longitudinal speed, with transverse and vertical velocities symmetrically distributed about zero. The overall bubble velocity is concentrated in the range of $0.25 \le U / U_0 \le 1$.

(5) At smaller submergence depths, the development of turbulence around the hydrofoil is suppressed. The vortex structures in the hydrofoil's wake mix with the vortices from the free surface breaking, resulting in the rapid fragmentation of larger bubbles and the downward sweeping of smaller bubbles to greater depths.

This study addresses aspects of free surface breaking and bubble dynamics that have received limited attention in previous research, providing useful insights for practical engineering applications such as near-surface propeller operation and hydrofoil vessels. In the future, it is necessary to investigate hydrofoils with varying angles of attack during motion to reveal how such movements influence free surface breaking. Additionally, the impact of free surface breaking on the lift and drag forces acting on the hydrofoil requires further examination.

Acknowledgements

This work was supported by the Research and Application Demonstration Project of Key Technologies for Safeguarding of Container vessels in Ningbo Zhoushan Port Based on Intelligent Navigation (Grant No. ZJHG-FW-2024-27).

Conflict of interest

All authors declare that there are no other competing interests.

References

[1] Deike L., Popinet S., Melville W. K. Capillary effects on wave breaking [J]. *Journal of Fluid Mechanics*, 2015, 769: 541-569.

[2] Deike L. Mass transfer at the ocean–atmosphere interface: the role of wave breaking, droplets, and bubbles [J]. *Annual Review of Fluid Mechanics*, 2022, 54(1): 191-224.

[3] McAllister M. L., Draycott S., Calvert R. et al. Three-dimensional wave breaking [J]. *Nature*, 2024, 633(8030): 601-607.

[4] Veron F. Ocean spray [J]. *Annual Review of Fluid Mechanics*, 2015, 47(1): 507-538.

[5] Stokes G. G. On the theory of oscillatory waves [J]. *Transactions of the Cambridge Philosophical Society*. 1847, 8: 441-455.

[6] Cartmill J. W., Su M. Y. Bubble size distribution under saltwater and freshwater breaking waves [J]. *Dynamics of Atmospheres and Oceans*, 1993, 20(1-2): 25-31.

[7] Deane G. B., Stokes M. D. Scale dependence of bubble creation mechanisms in breaking waves [J]. *Nature*, 2002, 418(6900): 839-844.

[8] Wang Z., Yang J., Stern F. High-fidelity simulations of bubble, droplet and spray formation in breaking waves [J]. *Journal of Fluid Mechanics*, 2016, 792: 307-327.

[9] Mostert W., Popinet S., Deike L. High-resolution direct simulation of deep water breaking waves: Transition to turbulence, bubbles and droplets production [J]. *Journal of Fluid Mechanics*, 2022, 942: A27.

[10] Liu W., Wang W., Qiu G. et al. KCS Unsteady bow wave breaking experiments for physics and CFD validation [C]. *34th Symposium on Naval Hydrodynamics (SNH)*, Washington DC, USA, 2022.

[11] Hu Y., Liu C., Hu C. et al. Numerical investigation of

flow structure and air entrainment of breaking bow wave generated by a rectangular plate [J]. *Physics of Fluids*, 2021, 33 (12): 122113.
[12] Hu Y., Liu C., Zhao M. et al. High-fidelity simulation of an aerated cavity around a surface-piercing rectangular plate [J]. *Physical Review Fluids*, 2023, 8(4): 044003.
[13] Li Z., Liu C., Wan D. et al. High-fidelity simulation of a hydraulic jump around a surface-piercing hydrofoil [J]. *Physics of Fluids*, 2021, 33 (12): 123304.
[14] Li Z., Liu C., Gao R. et al. A consistent mass-momentum advection method for the simulation of large-density-ratio two-phase flows [J]. *International Journal of Multiphase Flow*, 2022, 156: 104192.
[15] Hendrickson K., Yue D. K. P. Wake behind a three-dimensional dry transom stern. Part 2. Analysis and modelling of incompressible highly variable density turbulence [J]. *Journal of Fluid Mechanics*, 2019, 875: 884-913.
[16] Hendrickson K., Yue D. K. P. Structures and mechanisms of air-entraining quasi-steady breaking ship waves [J]. *Journal of Ship Research*, 2019, 63(02): 69-77.
[17] Zhang X., He K., Wan D. Research progress on mechanism and numerical simulation methods of water-air-bubble mixed flow around marine structure [J]. *Chinese Journal of Ship Research*, 2022, 17(3): 1-28
[18] Barkley D., Henderson R. D. Three-dimensional Floquet stability analysis of the wake of a circular cylinder [J]. *Journal of Fluid Mechanics*, 1996, 322: 215-241.
[19] Rao A., Leontini J., Thompson M. C. et al. Three-dimensionality in the wake of a rotating cylinder in a uniform flow [J]. *Journal of Fluid Mechanics*, 2013, 717: 1-29.
[20] Sheridan J., Lin J. C., Rockwell D. Flow past a cylinder close to a free surface [J]. *Journal of Fluid Mechanics*, 1997, 330: 1-30.
[21] Guo C., Ji M., Han Y. et al. Numerical simulation of the horizontal rotating cylinder and the air entrainment near the free surface [J]. *Physics of Fluids*, 2023, 35 (9): 092115.
[22] Duncan J. H. The breaking and non-breaking wave resistance of a two-dimensional hydrofoil [J]. *Journal of Fluid Mechanics*, 1983, 126: 507-520.
[23] Jin Q., Hudson D., Temarel P. et al. Turbulence and energy dissipation mechanisms in steady spilling breaking waves induced by a shallowly submerged hydrofoil [J]. *Ocean Engineering*, 2021, 229: 108976.
[24] Kennell C., Plotkin A. A second-order theory for the potential flow about thin hydrofoils [J]. *Journal of Ship Research*, 1984, 28(1): 55-64.
[25] Murai Y., Sakamaki H., Kumagai I. et al. Mechanism and performance of a hydrofoil bubble generator utilized for bubbly drag reduction ships [J]. *Ocean Engineering*, 2020, 216: 108085.
[26] Shao Y., Wang W., Wan D. et al. Numerical investigations of breaking waves and air entrainment induced by a shallowly submerged hydrofoil [J]. *Ocean Engineering*, 2024, 312: 119026.
[27] Popinet S. An accurate adaptive solver for surface-tension-driven interfacial flows [J]. *Journal of Computational Physics*, 2009, 228(16): 5838-5866.
[28] Popinet S. A quadtree-adaptive multigrid solver for the Serre–Green–Naghdi equations [J]. *Journal of Computational Physics*, 2015, 302: 336-358.
[29] Zhao W., Wang J., Wan D. Vortex identification methods in marine hydrodynamics [J]. *Journal of Hydrodynamics*, 2020, 32(2): 286-295.
[30] Rousta F., Ahmadi G., Lessani B. et al. Numerical study of the near-wall vortical structures in particle-laden turbulent flow by a new vortex identification method-Liutex [J]. *Journal of Hydrodynamics*, 2024, 36(1): 53-60.
[31] Hendrickson K., Weymouth G. D., Yu X. et al. Wake behind a three-dimensional dry transom stern. Part 1. Flow structure and large-scale air entrainment [J]. *Journal of Fluid Mechanics*, 2019, 875: 854-883.